Int. J. Electrochem. Sci., 7 **(2012)** 12340 - 12353

International Journal of
ELECTROCHEMICAL
SCIENCE
www.electrochemsci.org

Template-free Controlled Fabrication of $NH_4MnPO_4 \cdot H_2O$ and $Mn_2P_2O_7$ Micro-Nanostructures and Study of Their Electrochemical Properties

Huan Pang[1,2,3,*], *Zhenzhen Yan*[1], *Weiqiang Wang*[1], *Yuanyuan Wei*[1], *Xuexue Li*[1], *Juan Li* [1], *Jing Chen*[1], *Jiangshan Zhang*[1], *Honghe Zheng*[2,*]

[1] College of Chemistry and Chemical Engineering, Anyang Normal University, Anyang, 455000, Henan, P. R. China.
[2] School of Energy, Soochow University, Suzhou, 215006, Jiangsu, P. R. China.
[3] State Key Laboratory of Coordination Chemistry, Nanjing University, Nanjing, 210093, Jiangsu, P. R. China.
[*]E-mail: huanpangchem@hotmail.com; hhzheng@suda.edu.cn

Received: 24 August 2012 / *Accepted:* 3 October 2012 / *Published:* 1 December 2012

Various $NH_4MnPO_4 \cdot H_2O$ micro-nanostructures have been synthesized through a facile method without any surfactants or templates. All of the samples consist of the minimal basal unit nanosheet. Furthermore, porous micro-nanostructured manganous pyrophosphate ($Mn_2P_2O_7$) materials have been obtained by thermal decomposition of as-synthesized $NH_4MnPO_4 \cdot H_2O$ in the air. More importantly, we have successfully explored the application of micro-nanostructured $NH_4MnPO_4 \cdot H_2O$ and $Mn_2P_2O_7$ as electrochemical capacitors. The study of electrochemical measurements shows that micro-nanostructures affect their electrochemical properties. Different nano-microstructured $NH_4MnPO_4 \cdot H_2O$ and $Mn_2P_2O_7$ samples have different electrochemical properties.

Keywords: Micro-nanostructures; Thermal decomposition; Electrochemical measurement

1. INTRODUCTION

Recently, many efforts have been devoting to synthesize various micro-nanostructures, such as nanodots, nanorods, nanowires, nanoplates, nanospheres and three-dimensional ordered superstructures, due to their interesting properties of such micro-nanostructures and their potential applications in lots of fields [1-6], including catalysis [7], optoelectronics [8], lithium-ion batteries [9], drug delivery system [10], sensors [11, 12] and antibacterial agent [13, 14].However, methods to manipulation of these ordered structural materials have often need surfactants [15-17], copolymers [18,

19], and porous alumina as templates. Patterned-metal-catalyzed routes have also been used [20-22]. However, the main drawback of these methods is the need for complete template removal, otherwise impurities will exist in the final products [23-27]. Controlled solution-growth synthesis routes for the growth of inorganic materials are attractive because of the simplicity of the synthesis process. Therefore, there is significant interest in developing spontaneous generation of novel patterns with tailored structures and shapes by facile, hard template-free, solution-based, morphology controlled approaches to building novel self-generated micro-nanostructures.

Metal phosphates exhibit broad and potential applications in catalysis [29–32]. A preparation process has been used to synthesize an array of transition-metal phosphate amorphous colloidal spheres by Li et al [29]. Therefore, they have received considerable attention, and some progress has been made. Ammonium/transition metal phosphates have considerable industrially interesting properties. Ammonium phosphates of general formula $NH_4M^{II}PO_4 \cdot H_2O$ were first described in 1864 by Debray [33]. Carling and Yuan et al. obtained $NH_4M^{II}PO_4 \cdot H_2O$ (M^{II}=Mn, Fe, Co, and Ni) by precipitation from aqueous solution [34-35]. Zhang et al. have successfully reported a general method to prepare metal ammonium phosphate nanoflake constructed microspheres [36]. And Willem K. Kegel et al. have reported the preparation and characterization of colloidal particles of several pyrophosphate metal salts, including, for the first time, salts containing multiple metals [37].

Up to now, the development of alternative energy storage-conversion devices with high power and energy densities catering demands has increased to a greater extent [38]. Electrochemical capacitors have gained enormous attention due to their higher power density and longer cycle life compared to secondary batteries and higher energy density than conventional electrical double-layer capacitors [39, 40]. In particular, hydrous ruthenium oxides based materials exhibit much outstanding specific capacitance, longer cycle life than conventional materials [39, 41-47]. However, the high cost of this noble metal material limits it from commercialization and searching for alternative inexpensive electrode materials is indispensable.

In this work, we report that various micro-nanostructures $NH_4MnPO_4 \cdot H_2O$ have been successfully synthesized by a mild, simple chemical precipitation process without any surfactant at room temperature. The resulting material was subsequently determined to be the orthorhombic $NH_4MnPO_4 \cdot H_2O$. Furthermore, micro-nanostructured manganous pyrophosphate ($Mn_2P_2O_7$) materials with nanopores have been obtained by thermal decomposition of as-synthesized $NH_4MnPO_4 \cdot H_2O$ in the air. More importantly, there are nearly no reports about electrochemical capacitor of micro-nanostructured $NH_4MnPO_4 \cdot H_2O$ and $Mn_2P_2O_7$. We have successfully explored the application of nanostructured $NH_4MnPO_4 \cdot H_2O$ and $Mn_2P_2O_7$ as electrochemical capacitors. The study of electrochemical measurements shows that micro-nanostructures affect their electrochemical properties.

2. EXPERIMENTAL PART

2.1 Preparation of $NH_4MnPO_4 \cdot H_2O$ Micro-nanostructures

$NH_4MnPO_4 \cdot H_2O$ micro-nanostructures, M1-M3 and M6: Manganous chloride ($MnCl_2 \cdot 4H_2O$) and ammonium phosphate ($(NH_4)_3PO_4 \cdot 3H_2O$) were used as manganese cation and phosphate anion

precursors, respectively. Typically, 3.0 g of ammonium chloride and 0.2 g of ammonium phosphate was added to a beaker and then 40 mL ethylene glycol (M1) or 20 mL water and 20 mL ethylene glycol (M2), or 20 mL water and 20 mL glycerol (M3), or 20 mL water and 20 mL polyethylene glycol (M6) was added. Mixture was stirred at room temperature until solid were completely dissolved. Then, 0.2 g $MnCl_2 \cdot 4H_2O$ was added to mixed solution and vigorous magnetic stirring at room temperature for 12 h. The obtained homogeneous white precipitates were washed with deionized water and ethanol several times and dried.

$NH_4MnPO_4 \cdot H_2O$ micro-nanostructures, M4-M5: 3.0 g of ammonium phosphate was added to a beaker and then 80 mL ethylene glycol (M4) or 40 mL ethylene glycol (M5) was added. Mixture was stirred at room temperature until solid were completely dissolved. Then, 0.2 g $MnCl_2 \cdot 4H_2O$ was added to the mixed solution and vigorous magnetic stirring at room temperature for 12 h. The subsequent synthesis procedure was the same as that described above.

2.2 Preparation of $Mn_2P_2O_7$ Micro-nanostructures

Various $Mn_2P_2O_7$ micro-nanostructures (which were named P1-P6 corresponding to M1-M6) were prepared by heating the corresponding $NH_4MnPO_4 \cdot H_2O$ micro-nanostructures (M1-M6) in air at 500 ^oC for 10 min at a heating rate of 1 ^oC/ min.

2.3 Electrode Preparation

The working electrodes were prepared as follows. The electrode of $NH_4MnPO_4 \cdot H_2O$ or $Mn_2P_2O_7$ materials were prepared according to the following steps. The mixture containing 80 wt.% $NH_4MnPO_4 \cdot H_2O$ or $Mn_2P_2O_7$ materials, 15 wt.% acetylene black and 5 wt.% polytetrafluoroethylene (PTFE) was well mixed, and then was pressed onto nickel grid (1.2×10^7 Pa) that serves as a current collector (surface is 1 cm^2). The typical mass load of electrode material is about 5 mg.

2.4 Characterization

The morphology of the as-prepared samples was observed by a JEOL JSM-6701F field-emission scanning electron microscope (FE-SEM) at an acceleration voltage of 5.0 kV. Transmission electron microscopy (TEM) images. The phase analyses of the samples were performed by X-ray diffraction (XRD) on a Ultima III with Cu K_α radiation (λ = 1.5418 Å). Thermogravimetric analysis (TG) was carried out on the microspheres in air up to 800 °C using a NETZSCH STA 409 PC instrument with a heating rate of 5 °C/min. The cyclic voltammogram (CV) were measured on an electrochemical station-CHI 660d. And electrochemical impedance spectroscopy (EIS) measurements of all the samples were conducted at open circuit voltage in the frequency range of 100 kHz to 0.01 Hz with AC voltage amplitude of 5 mV using PARSTAT2273.

3. RESULTS AND DISCUSSION

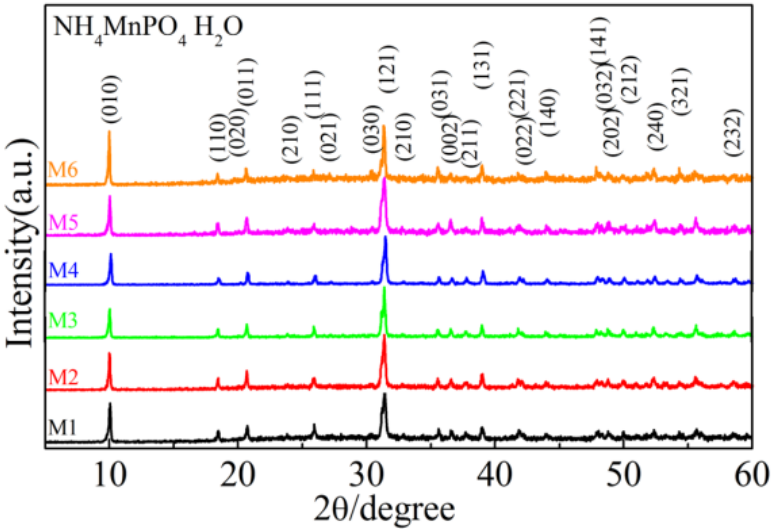

Figure 1. the powder X-ray diffraction patterns of M1-M6.

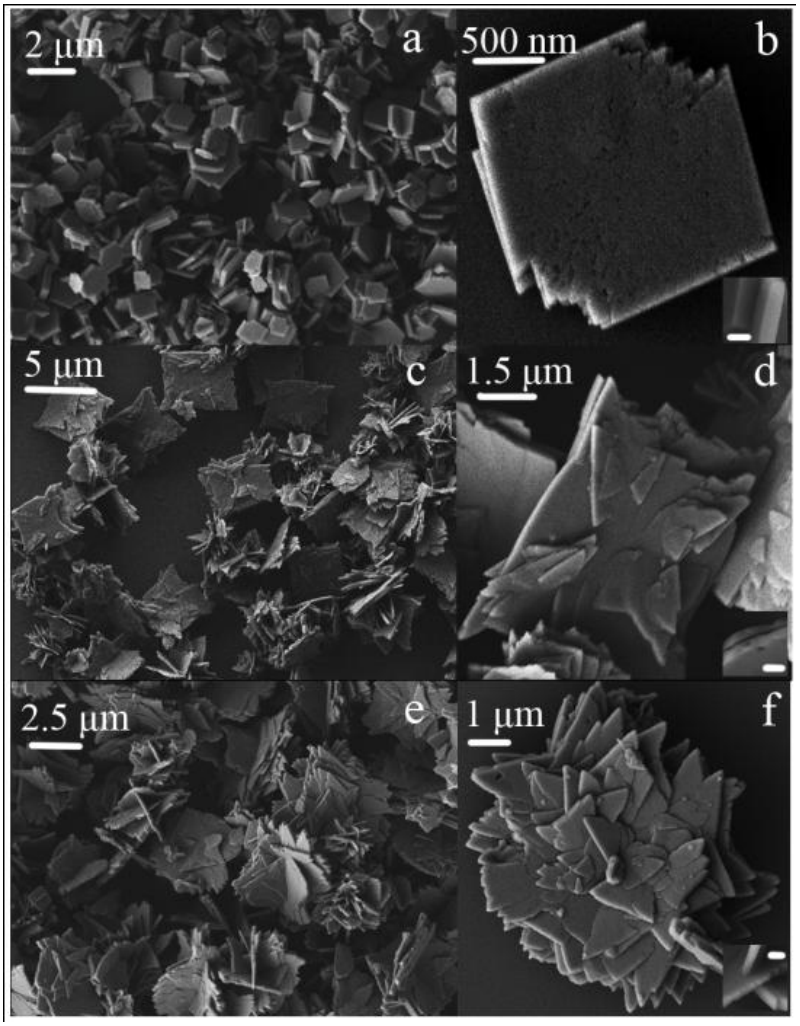

Figure 2. SEM images of $NH_4MnPO_4 \cdot H_2O$ micro-nanostructures, (a-b) M1; (c-d) M2; (e-f) M3.

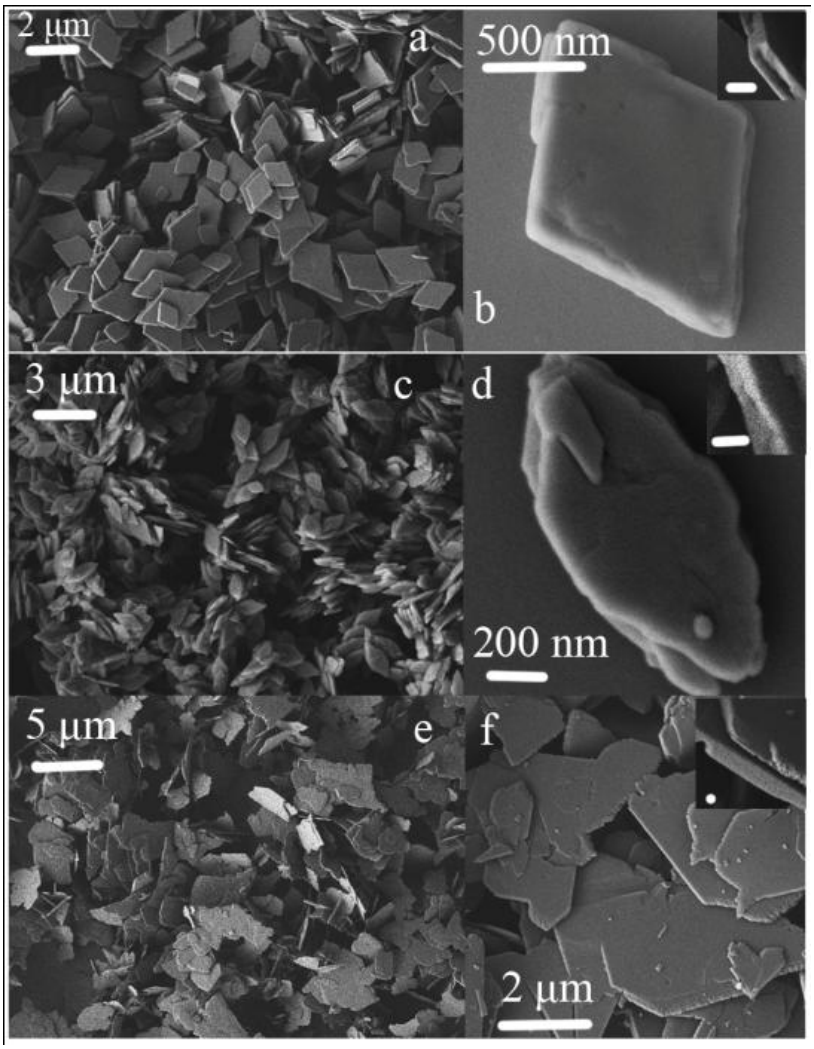

Figure 3. SEM images of $NH_4MnPO_4 \cdot H_2O$ micro-nanostructures, (a-b) M4; (c-d) M5; (e-f) M6.

Fig. 1 shows XRD patterns of various $NH_4MnPO_4 \cdot H_2O$ nanostructure precursors. From Fig. 1, all the diffraction peaks from M1-M6 can be indexed to $NH_4MnPO_4 \cdot H_2O$, JCPDS card 50-0554, which shows that the product is orthorhombic $NH_4MnPO_4 \cdot H_2O$. The sharp diffraction peaks without those for any impurity phases such as $Mn_3(PO_4)_2$ and others, which often appear in the NH_4MnPO_4 product synthesized by other routes, illustrate the good crystalline nature of NH_4MnPO_4 achieved by the chemical precipitation process at room temperature.

The size and shape of as-prepared $NH_4MnPO_4 \cdot H_2O$ were examined by field emission scanning electron microscopy (FE-SEM). Fig. 2 and Fig. 3 show FE-SEM images of $NH_4MnPO_4 \cdot H_2O$ samples obtained with different conditions. FE-SEM images of M1 are showed in Fig. 2a-b. It indicates that the sample almost completely consists of angle-cut cubic plate structures, which are uniform with diameter of 1-2 μm. In inset of Fig. 2b, we can see the thickness of angle-cut cubic flake structure is about 200 nm. From images of Fig. 2c-d, we can see that nanoplates have made up of microplate-M2, whose diameter is in the range of 6-7 μm. FE-SEM images of M3 were showed in Fig. 2e-f, in which we can see $NH_4MnPO_4 \cdot H_2O$ are formed in a large scale with relatively uniform diameters of 6–7 μm microflowers assembled by many nanoplates, and the nanoplate has an average thickness of 200 nm in

inset of Fig. 2f. We can find that the morphology of M2 is similar to M3 except assemble plate forms due to using different solvents. Glycerine is a much more sticky solvent compared with common solvents, water and ethanol. The high-viscosity glycerine may slow down the ion diffusion rate and thus prevent the particle from growing or assembling. And then M1 shows single plate morphology due to using only ethylene glycol as solvent without adding water.

The viscosity of solvent might have influence on the particle shape. When we used pure ethylene glycol as solvent, smaller plate morphology can be obtained. From FE-SEM images in Fig. 3a-b, it revealed nearly uniform diamond nanoplate $NH_4MnPO_4 \cdot H_2O$ (M4) and the diamond nanoplate has an average size about 2 μm. The thickness is about 100 nm in inset of Fig. 3b. From Fig. 3 c-d, it consists of a large number of fairly uniform particles. It almost completely consists of spindle nanoplate structures with an average size of about 1 μm (M5) and 100 nm of thickness. When using water-polyethylene glycol mixed solvent, we can seen that the morphology of $NH_4MnPO_4 \cdot H_2O$ has transform into formless large microplates with 200 nm of thickness from several micrometers to dozens of micrometers (M6). It is obvious that the thickness of $NH_4MnPO_4 \cdot H_2O$ is much thicker than others.

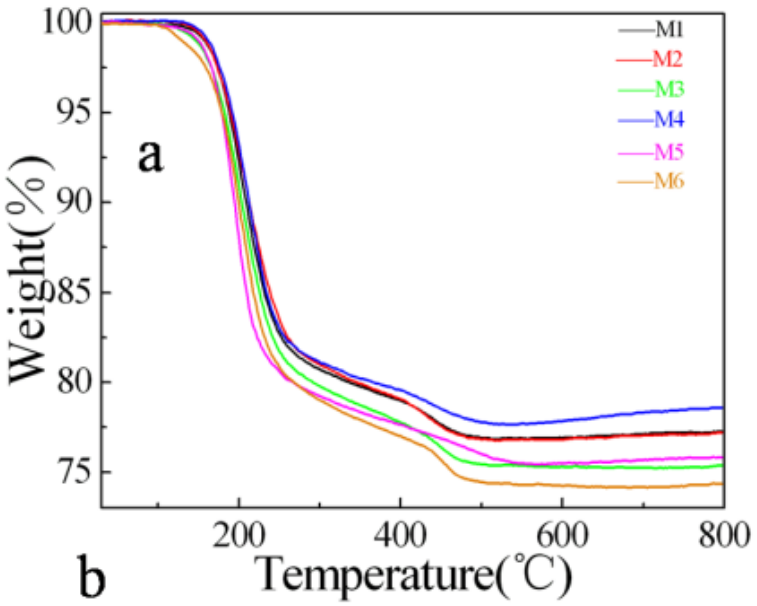

Figure 4. (a) TG curves of $NH_4MnPO_4 \cdot H_2O$ and (b) Chemical reaction equation of $NH_4MnPO_4 \cdot H_2O$s' decomposition.

Fig. 4 a shows TG curves of $NH_4MnPO_4 \cdot H_2O$ (M1-M6) were measured from room temperature to 800 ^oC. The curves show that the thermal decomposition of various $NH_4MnPO_4 \cdot H_2O$ nanostructure precursors below 800 ^oC occurs in two weight loss steps. The first weight loss step is between 130 ^oC and 250 ^oC. It could be due to a water molecule and ammonia eliminated from $NH_4MnPO_4 \cdot H_2O$ and the formation of $MnHPO_4$. The observed weight loss on the TG curve is 18.4%, which is in good

agreement with 18.84% theoretic weight loss of a water molecule and ammonia eliminated from $NH_4MnPO_4 \cdot H_2O$. Moreover, the second decomposition step begins at 250 ^oC and ends at 500 ^oC, attributable to the dehydration of $MnHPO_4$ and the formation of $Mn_2P_2O_7$. The corresponding observed weight loss on the TG curve is 4.99%, which is close to 4.84% theoretic weight loss of half a water molecule eliminated from $MnHPO_4$. The chemical reaction equation of the decomposition can be seen in Fig. 4b.

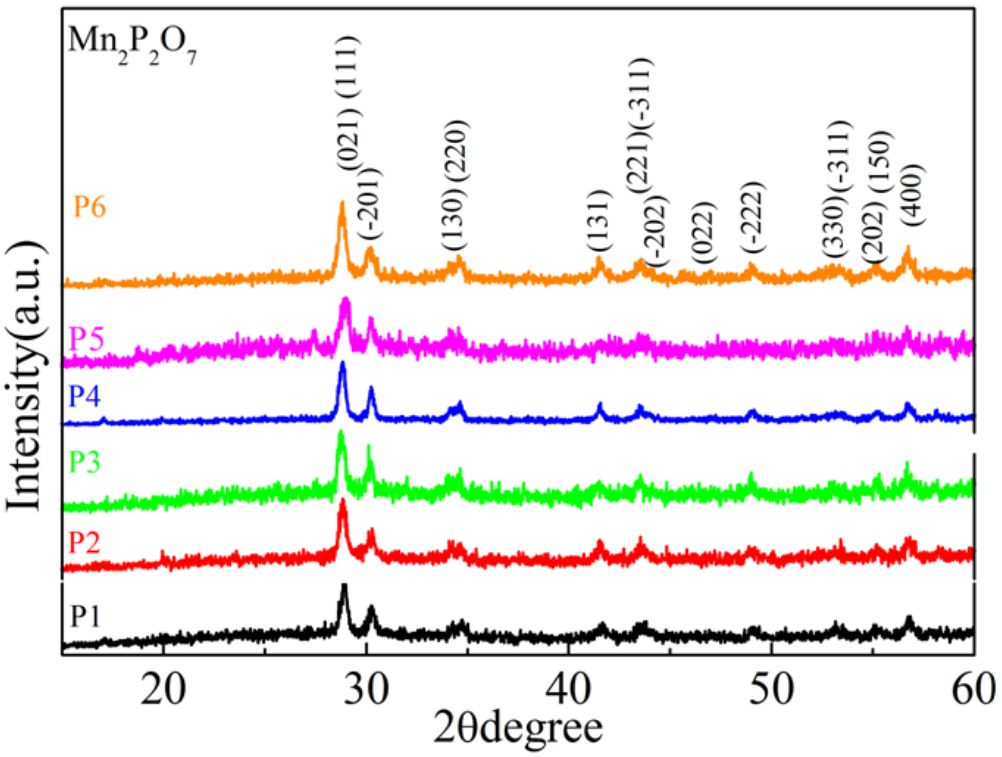

Figure 5. the powder X-ray diffraction patterns of P1-P6.

Fig. 5 shows XRD patterns of all the $Mn_2P_2O_7$ samples. All of the reflection peaks in the XRD patterns match well with the standard pattern of cubic $Mn_2P_2O_7$ (JCSPDF card No: 29-0891). After heated treatment at 500 ^oC for 10 min, $NH_4MnPO_4 \cdot H_2O$ micro-nanostructures have transformed into porous $Mn_2P_2O_7$ micro-nanostructures. Powder XRD characterizations confirm that $Mn_2P_2O_7$ micro-nanostructures have successfully been obtained under our experimental conditions with good purity.

Fig. 6 display FESEM images of $Mn_2P_2O_7$ samples (P1-P3). Fig. 6a is a low magnification FESEM image of sample P1. It is seen that the product maintained the shape of M1 precursor and showed angle-cut cubic plate structures. An FESEM image with high magnification is shown in Fig. 6b. Unlike M1, P1 have porous structures which might be caused by decomposition of M1 and the releasing gases in Fig. 6b. During the calcination process from $NH_4MnPO_4 \cdot H_2O$ to $Mn_2P_2O_7$, the loss of water and ammonia would cause the shrinkage and a different shrinkage velocity at different parts of materials would lead to the formation of these pores. Fig. 6c and d show SEM images of P2, which be obtained from calcination of M2. In Fig. 6c, the images indicate that porous assemble $Mn_2P_2O_7$

microplates P2 preserving the shape of M2, which are around 6-7 μm. Porous $Mn_2P_2O_7$ microplates can be easily obtained by calcining M1, which is made up of many porous plates.

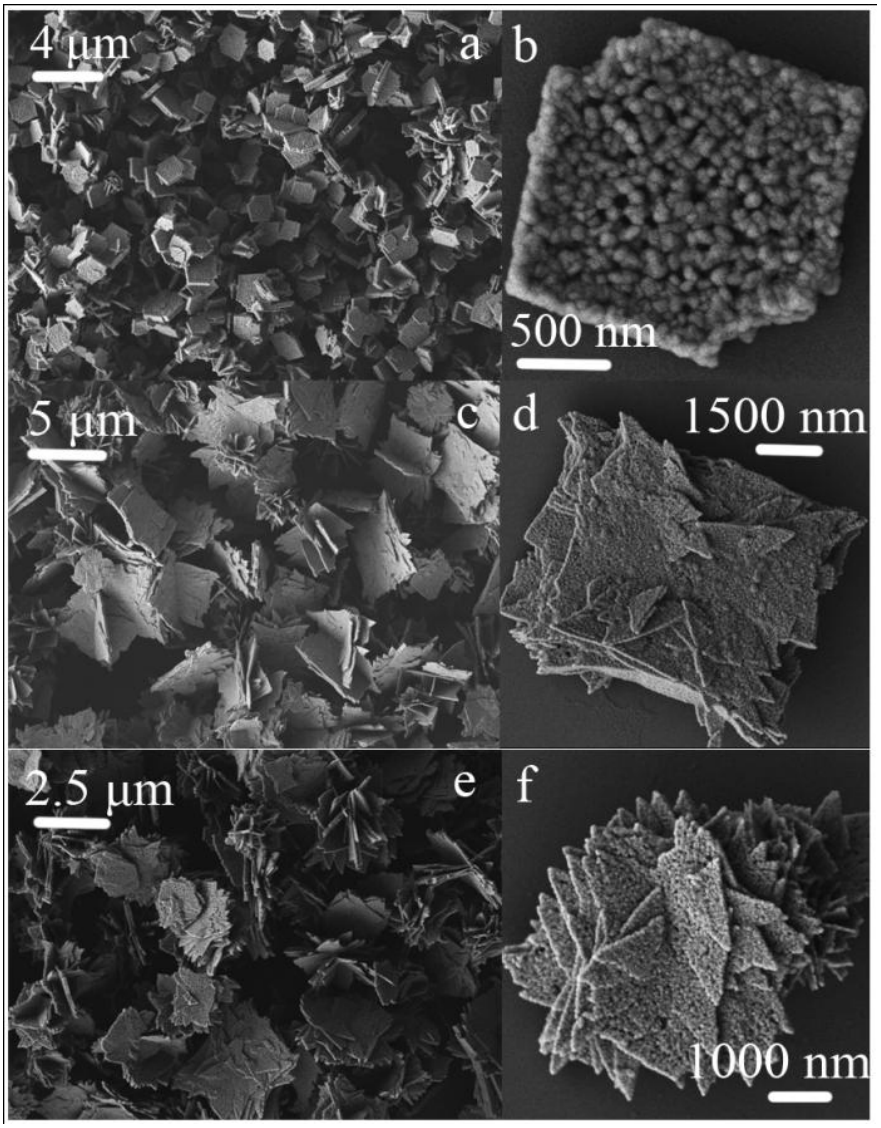

Figure 6. SEM images of $Mn_2P_2O_7$ micro-nanostructures: (a-b) P1; (c-d) P2; (e-f) P3.

In Fig. 7a, we can see that porous diamond nanoplates in large scale (named P4). And a lot of $Mn_2P_2O_7$ nanoparticles formed a single porous diamond nanoplate within about 1.5 μm in Fig. 7b. Porous $Mn_2P_2O_7$ spindle nanoplates were also obtained easily by calcining the $NH_4MnPO_4{\cdot}H_2O$ spindle nanoplate within about 1 μm (named P5) in Fig. 7c-d. Large $Mn_2P_2O_7$ microplates can be seen in Fig. 7e, unlike others we can see the surface of P6 is much smoother, which means such $Mn_2P_2O_7$ microplates are quite solid in Fig. 7f (named P6).

The electrochemical measurements of all samples were performed in 1.0 mol L^{-1} aqueous Na_2SO_4 aqueous solution using three-electrode cells. Cyclic voltammetry (CV) measurements were

used to evaluate the electrochemical properties and quantify the specific capacitance of as-prepared samples electrodes.

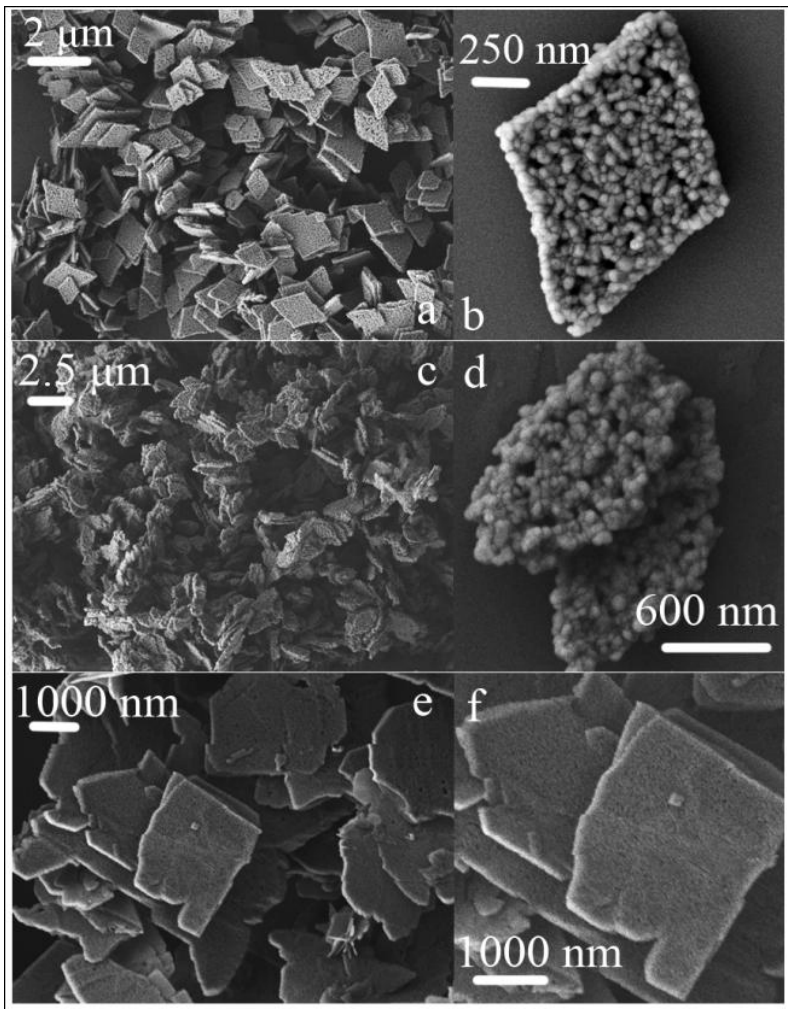

Figure 7. SEM images of $Mn_2P_2O_7$ micro-nanostructures: (a-b) P4; (c-d) P5; (e-f) P6.

A capacitor in a Na_2SO_4 solution relies on charge storage in the electric double layer at the electrode–electrolyte interface and charge storage in the host material through redox reactions on the surface and sodium ion diffusion in the host material [38, 39]. Fig. 8a shows the CV curves of M1-M6 at 20 mV s^{-1} scan rate, and Fig. 8b shows the CV curves of P1-P6 at 20 mV s^{-1} scan rate. CV curves in Fig. 8a-b show the normal regular shape and the different leveled current separations between leveled anodic and cathodic currents suggest effective electrochemical performance of electrode material.

Specific capacitance of micro-nanostructures electrodes at different scan rates was shown in Fig. 8c-d. At the scan rate of 10 mV s^{-1}, the specific capacitance of M3 electrodes can achieve 35 F g^{-1} (based on the mass of $NH_4MnPO_4 \cdot H_2O$), and that of P3 electrodes are 31 F g^{-1} (based on the mass of $Mn_2P_2O_7$), while those of others electrodes shown low specific capacitance. Even though the specific capacitance of M3 drops as the scan rate increases, the specific capacitance of M3 still retained, about 17 F g^{-1} at the scan rate of 100 mV s^{-1}. The drop can be explained by the ion-exchange mechanism.

The Na^+ needs enough time to transfer between the solution into the surface of electrode material in order to be intercalated/extracted into/out of the electrode material when charging/discharging.

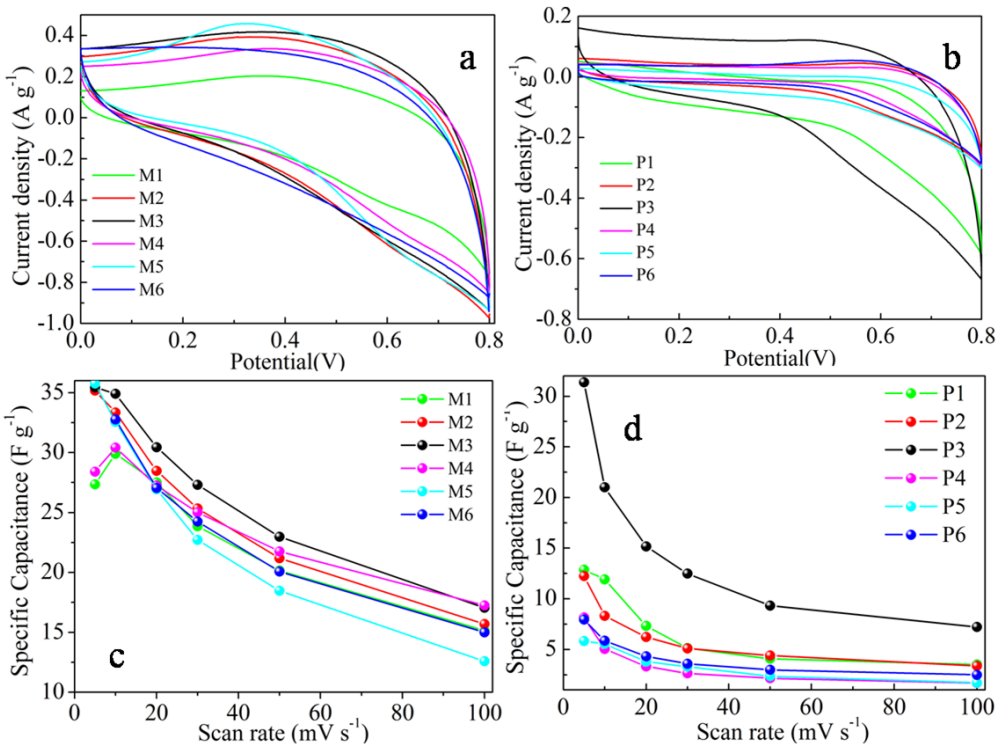

Figure 8. (a) CV curves of M1-M6 at 20 mV s^{-1} scan rate; (b) CV curves of P1-P6 at 20 mV s^{-1} scan rate; (c) specific capacitance of M1-M6 electrodes at 5, 10, 20, 30, 50, 100 mV s^{-1} scan rate; (d) specific capacitance of P1-P6 electrodes at 5, 10, 20, 30, 50, 100 mV s^{-1} scan rate.

If the scan rate is low, such as 5 mV s^{-1}, the Na^+ can have enough time to transfer and much more charge transfers than at a high scan rate, which means more charge can be stored and thus higher specific capacitance. The CV tests suggest that, the electrochemical accessible surface area of electrode material is increased due to the large surface to volume ratio of micro-nanostructures (BET can be seen in Table 1), resulting in the effective improvement of the specific capacitance. Additionally, the electrochemical performance could be further improved after optimization of the synthesis conditions

We proposed the possible mechanism (eq. 1 and eq. 2) to explain the intercalation/deintercalation of Na^+ in various NH_4MnPO_4 and $Mn_2P_2O_7$ materials.

$$NH_4MnPO_4 + Na^+ + e^- === NaNH_4MnPO_4; \quad \text{(eq.1)}$$

$$Mn_2P_2O_7 + Na^+ + e^- === NaMn_2P_2O_7; \quad \text{(eq.2)}$$

To understand the electrode kinetics, the activation energies of the as-prepared materials for Na^+ intercalation were estimated by electrochemical impedance spectra (EIS). Fig. 9 shows the EIS of

different electrodes. In general, the impedance curves present two partially overlapped semicircles in the high- and medium-frequency regions and an inclined line in the low-frequency region.

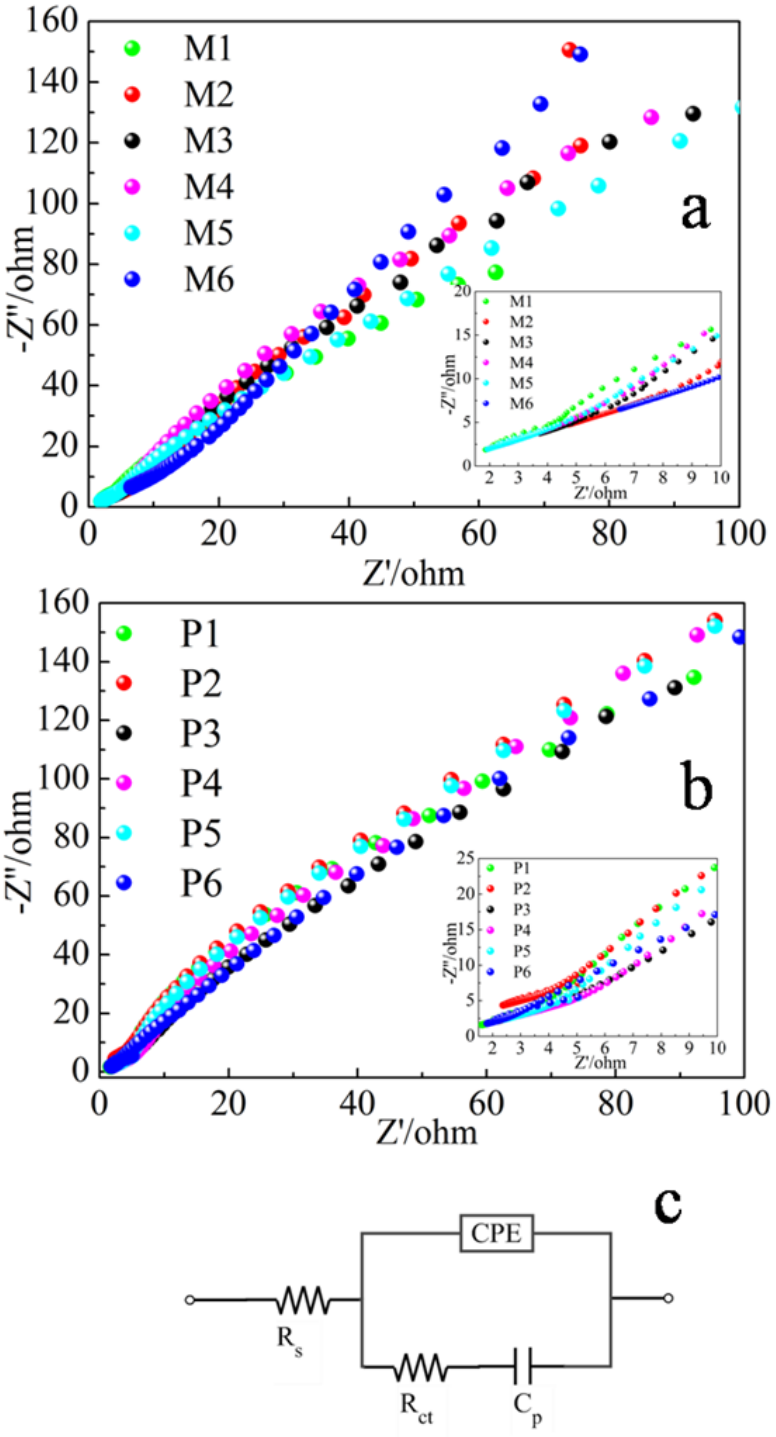

Figure 9. Electrochemical impedance spectra (EIS) for $NH_4MnPO_4 \cdot H_2O$ and $Mn_2P_2O_7$ electrodes under room temperature in 1.0 M Na_2SO_4 solution at 0.8 V, (a) M1-M6; (b) P1-P6; (c) An equivalent circuitan consisting of a bulk solution resistance R_s, a charge-transfer R_{ct}, a pseudocapacitive element C_p from redox process of $NH_4MnPO_4 \cdot H_2O$ and $Mn_2P_2O_7$, and a constant phase element (CPE) to account for the double-layer capacitance.

Table 1. Brunauer-Emmett-Teller (BET) measurements of samples.

Sample	BET m^2/g	Sample	BET m^2/g
M1	7	P1	8.2
M2	7.5	P2	7.8
M3	10.6	P3	15.6
M4	8.5	P4	5.2
M5	5.4	P5	5.2
M6	6.3	P6	6.8

Table 2. A charge-transfer R_{ct} was calculated by ZSimpWin software based on Fig. 9.

Sample	R_{ct}/ohm	Sample	R_{ct}/ohm
M1	36	P1	46.2
M2	38	P2	42.1
M3	20.5	P3	30.6
M4	31.5	P4	50.1
M5	42.6	P5	61
M6	40.7	P6	61.8

An equivalent circuit used to fit the impedance curve is given in Fig. 9c, which is similar to the circuit employed for the working electrode of supercapacitor. The EIS data can be fitted by a bulk solution resistance R_s, a charge-transfer R_{ct} and a pseudocapacitive element C_p from redox process of materials, and a constant phase element (CPE) to account for the double-layer capacitance. The charge-transfer resistance R_{ct} was calculated by ZSimpWin software which can be seen in Table 2, respectively. This clearly demonstrates the reduced charge transfer resistance of the M3 electrode. In addition, the charge-transfer resistance R_{ct}, also called Faraday resistance, is a limiting factor for the specific power of the supercapacitor [41]. It is the low Faraday resistance that results in the high specific power of M3 electrode. The charge-transfer resistance R_{ct} of the M3 electrode is the lowest of all, which makes high electric activity. More importantly, nanostructured M3 allows ions or electrolyte transfer to occur quickly.

4. CONCLUSIONS

In this work, different $NH_4MnPO_4 \cdot H_2O$ micro-nanostructures have been synthesized through a facile method without any assistance of surfactants or templates. All of the samples consist of minimal basal unit, the nanosheet. The solvent has the great influence on the formation of $NH_4MnPO_4 \cdot H_2O$ micro-nanostructures with different assembly modes. The micro-nanostructures can be well preserved during the thermal transformation from $NH_4MnPO_4 \cdot H_2O$ to $Mn_2P_2O_7$. Because of the different morphologies, different nanostructured $Mn_2P_2O_7$ samples have different electrochemical properties.

Further studies of the construction of NH_4MnPO_4 and $Mn_2P_2O_7$ micro-nanostructures would bring new insight into the morphology–property relationship.

ACKNOWLEDGMENT
This work is supported by the National Natural Science Foundation of China (21201010, 21073129, 21071006), the Department of Science and technology of China for the 863 project (2009AA03Z225863). Henan Province of Science & Technology Foundation (122102210253) and the project of Science & Technology of Anyang city.

References

1. H. Pang, Q. Y. Lu, Y. Z. Zhang, Y. C. Li, F. Gao, *Nanoscale*, 2 (2010) 920
2. H. Pang, B. Zhang, J. Du, J. Chen, J. S. Zhang, S. Li, *RSC Adv*., 2 (2012) 2257
3. H. Pang, F. Gao, Q. Y. Lu, *Chem. Commun*., (2009) 1076
4. H. Pang, Q. Y. Lu, J. J. Wang, Y. C. Li, F. Gao, *Chem. Commun*., 46 (2010) 2010
5. H. Pang, F. Gao, Q. Y. Lu, *Chem. Commun*., 47 (2011) 11772
6. H. Pang, Q. Y. Lu, Y. C. Li, F. Gao, *Chem. Commun*., (2009) 7542
7. C. Burda, X. B. Chen, R. Narayanan, M. A. El-Sayed, *Chem. Rev.*, 105 (2005) 1025
8. X. Duan, Y. Huang, Y. Cui, J. Wang, C. M. Lieber, *Nature*, 409 (2001) 66
9. A. M. Cao, J. S. Hu, H. P. Liang, L. J. Wan, *Angew. Chem. Int. Ed.*, 44 (2005) 4391
10. Y. Cai, H. Pan, X. Xu, Q. Hu, L. Li, R. Tang, *Chem. Mater*., 19 (2007) 3081
11. D. F. Zhang, L. D. Sun, G. Xu, C. H. Yan, *Phys. Chem. Chem. Phys.*, 8 (2006) 4874
12. F. Favier, E. C. Walter, M. P. Zach, T. Benter, R. M. Penner, *Science*, 293 (2001) 2227
13. T. Zhang, W. Dong, M. Keeter-Brewer, K. Sanjit, R. N. Njabon, Z. R. Tian, *J. Am. Chem. Soc.*, 128 (2006) 10960
14. S. H. Yu, M. Yoshimura, *Adv. Mater*., 14 (2002) 296
15. L. Manna, D. J. Milliron, A. Meisei, E. C. Scher, A. P. Alivisatos, *Nat. Mater*., 2 (2003) 382
16. Y. W. Jun, Y. Y. Jung, J. Cheon, *J. Am.Chem. Soc.*, 124 (2002) 615
17. T. K. Sau, C. J. Murphy, *J. Am. Chem. Soc*., 126 (2004) 8648
18. S. H. Yu, H. Cölfen, M. Antonietti, *Chem. Eur. J*., 8 (2002) 2937
19. L. Q. H. Cölfen, M. Antonietti, M. Li, J. D. Hopwood, A. J. Ashley, S. Mann, *Chem. Eur. J.*, 7 (2001) 3526
20. B. T. Holland, C. F. Blanford, A. Stein, *Science*, 281 (1998) 538
21. H. Cao, Y. Xu, J. Hong, H. Liu, G. Yin, B. Li, C. Tie, Z. Xu, *Adv. Mater.*, 13 (2001) 1393
22. T. Martensson, P. Carlberg, M. Borgström, L. Montelius, W. Seifert, L. Samuelson, *Nano Lett.*, 4 (2004) 699
23. R. Ma, Y. Bando, L. Zhang, T. Sasaki, *Adv. Mater*., 16 (2004) 918
24. X. Wang, Y. Li, *Chem. Eur. J.*, 9 (2003) 300
25. X. Wang, Y. Li, *J. Am. Chem. Soc.*, 124 (2002) 2880
26. X. F. Shen, Y. S. Ding, J. Liu, J. Cai, K. Laubernds, R. P. Zerger, A. Vasiliev, M. Aindow, S. L. Suib, *Adv. Mater.*, 17 (2005) 805
27. P. Levy, A. G. Leyva, H. E. Troiani,d R. D. Sanchez, *Appl. Phys. Lett.*, 83 (2003) 5247.
28. F. S. Xiao, J. M. Sun, X. J. Meng, R. B. Yu, H. M. Yuan, D. Z. Jiang, S. L. Qiu, R. R. Xu, *Appl. Catal., A*, 207 (2001) 267
29. C. Chen, W. Chen, J. Lu, D. Chu, Z. Huo, Q. Peng, Y. Li, *Angew. Chem., Int. Ed.*, 48 (2009) 4816
30. C. Morgovan, E. Marian, A. Iovi, I. Bratu, G. Borodi, *Rev. Chim.*, 60 (2009) 1282
31. H. Jiang, T. Zhao, C. Li, J. Ma, *J. Mater. Chem.*, 21 (2011) 3818
32. I.-S. Cho, D. W. Kim, S. Lee, C. H. Kwak, S. T. Bae, J. H. Noh, S. H. Yoon, H. S. Jung, D.-W. Kim, K. S. Hong, *Adv. Funct. Mater.*, 18 (2008) 2154

33. C. Debray, *R. Acad. Sci*., 59 (1864) 40
34. S. G. Carling, P. Day, D. Visser, *Inorg. Chem*., 34 (1995) 3917
35. A. Q. Yuan, J. Wu, L. J. Bai, S. M. Ma, Z. Y. Huang, Z. F. Tong, *J. Chem. Eng. Data*., 53 (2008) 1066
36. C. F. Zeng, W. W. Ji, L. X. Zhang, *CrystEngComm*, 14 (2012) 3008
37. Y. M. Leeuwen, K. P. Velikov, W. K. Kegel, *RSC Adv*., 2 (2012) 2534
38. V. Subramanian, H. Zhu, R. Vajtai, P. M. Ajayan, B. Wei, *J. Phys. Chem. B*, 109 (2005) 20207
39. S. Sarangapani, B. V. Tilak, C. P. Chen, *J. Electrochem. Soc.*, 143 (1996) 3791
40. R. N. Reddy, R. G. Reddy, *J. Power Sources*, 132 (2004) 315
41. B. E. Conway, *Electrochemical Supercapacitors*; Kluwer Academic/Plenum Publishers: New York, 1999
42. C. C. Hu, C. C. Wang, *Electrochem. Commun.*, 4 (2002) 554
43. Z. J. Zhang, Z. L. Wang, B. C. Chakoumakos, J. S. Yin, *J. Am. Chem. Soc.*, 120 (1998) 1800.
44. X. Xia, J. Tu, X. Wang, C. Gu, X. Zhao, *J. Mater. Chem.*, 21 (2011) 671–679.
45. Y. Gao, S. Chen, D. Cao, G. Wang, J. Yin, *J. Power Sources*, 195 (2010) 1757–1760.
46. C. Z. Yuan, X. G. Zhang, L. H. Su, B. Gao, L. F. Shen, *J. Mater. Chem.*, 19 (2009) 5772–5777.
47. R. Barnard, C. F. Randell, F. L. Tye, *J. Appl. Electrochem.*, 10 (1980) 109-116.